The axial form factor of the nucleon with Padé approximants

Author: Laia Asiain Peracaula, lasiaipe7@alumnes.ub.edu
Facultat de Física, Universitat de Barcelona, Diagonal 645, 08028 Barcelona, Spain.

Advisor: Sergi Gonzàlez-Solís de la Fuente, sergig@fqa.ub.edu

Abstract: This work explores the axial-vector form factor of the nucleon, $F_A(Q^2)$, using Padé approximants as a model-independent alternative to the traditional dipole ansatz. This method allows us to incorporate the $a_1(1260)$ resonance to the parametrization of $F_A(Q^2)$ while also systematically improving the approximation with higher-order Padé terms as more precise data becomes available, thereby reducing theoretical uncertainties. We fit data from Lattice QCD simulations and pion electroproduction experiments to extract the mean squared axial radius, $\langle r_A^2 \rangle$. The resulting values are $\langle r_A^2 \rangle = (0.268 \pm 0.010)\,\mathrm{fm}^2$ for the Lattice QCD predictions, $\langle r_A^2 \rangle = (0.405 \pm 0.009)\,\mathrm{fm}^2$ for the pion electroproduction data and $\langle r_A^2 \rangle = (0.324 \pm 0.006)\,\mathrm{fm}^2$ for the combined datasets. Finally, we compare our results with determinations from quasielastic neutrino-nucleon scattering cross section $\nu_\mu n \to \mu p$ experimental data analyses.
Keywords: Axial-vector form factor, Padé approximants, Lattice QCD, Nucleon structure
SDGs: Quality education

I. INTRODUCTION

The accurate study of lepton-nucleon interactions requires a precise calculation of the scattering cross section, which depends directly on the nucleon's form factors. Although the electromagnetic form factors of the proton — and to a lesser extent, the neutron — have been measured with high precision, our understanding of those associated with the isovector axial-vector current remains limited. In particular, the axial form factor F_A and the induced pseudoscalar form factor F_P are considerably less well determined.

The analysis of the axial-vector form factor poses challenges both experimentally and theoretically. Since it can only be accessed through weak interaction, direct measurements are limited to low-statistics neutrino-nucleus scattering and pion electroproduction experiments. The former are affected by substantial nuclear effects, while the latter are restricted by model-dependent corrections. On the theoretical side, the form factor is usually described using a dipole ansatz. Nonetheless, recent discrepancies between various experimental results and Lattice QCD predictions have raised questions about the validity of this approach. Among these inconsistencies, we find tension between measurements of the charged current quasielastic neutrino-nucleon scattering cross section $\nu_\mu n \to \mu p$ at low and high neutrino energies, between results from neutrino-nucleon scattering cross section and results based on the analysis of data from pion electroproduction $\gamma^* N \to \pi N$, and between the latter and recent Lattice QCD predictions.

One possible explanation to these contradictions is that the dipole parametrization is simply too constrained to be able to provide a complete description of the axial-vector form factor. This model is purely empirical, with no underlying theoretical justification beyond its fit to the experimental measurements.

Using data from pion electroproduction experiments [1] and Lattice QCD predictions [2, 3], this work aims to provide a more flexible, data-driven method to the modelling of the axial-vector form factor using Padé approximants [4]. Since this is a systematic approach, Padé approximants present great adaptability to the future addition of higher-precision data, as they allow for higher-order approximations that reduce the uncertainties in the results obtained.

This work is structured as follows. The theoretical background is discussed in Secs. II and III. In the first one we present the axial form factor and its most common parametrization, along with some axial mass and radius values obtained in different collaborations, while in the latter Padé approximants and their main advantages over Taylor series are discussed. Sec. IV contains a brief explanation on the process of extracting the mean squared axial radius from PA fittings to experimental and Lattice QCD data, the final results and the criteria used to discard certain outputs. The closing section contains a brief summary of the study performed and the results obtained (Sec. V).

II. THE AXIAL-VECTOR FORM FACTOR OF THE NUCLEON

The electroweak form factors are functions that describe the internal structure of the nucleon. They are of particular interest in high-precision neutrino measurements — such as those related to oscillation parameters, mass hierarchy, and CP violation — as they allow us to compute the cross section.

Mathematically, form factors emerge from the matrix elements of the electroweak current operators evaluated between initial and final nucleon states. For the electro-

magnetic current, this leads to the expression:

$$\langle N(p')|J^{\mu}_{\rm EM}|N(p)\rangle = \bar{u}(p')\Big[\gamma^{\mu}F_1(q^2)+ + \frac{i}{2m_N}\sigma^{\mu\nu}q_{\nu}F_2(q^2)\Big]u(p), \quad (1)$$

where $q = p' - p$ is the momentum transfer and m_N denotes the nucleon mass. $F_1(q^2)$ and $F_2(q^2)$ are the electric and magnetic form factors respectively (also known as Dirac and Pauli form factors), and they are well known across a broad range of q^2.

On the other hand, the matrix element of the isovector axial-vector current is given by:

$$\langle N(p')|J^{\mu a}_{\rm A}|N(p)\rangle = \bar{u}(p')\frac{\tau^a}{2}\gamma_5\Big[\gamma^{\mu}F_A(q^2)+ + \frac{q^{\mu}}{2m_N}F_P(q^2)\Big]u(p), \quad (2)$$

with τ^a being Pauli matrices and $F_A(q^2)$ and $F_P(q^2)$ being the axial form factor and the induced pseudoscalar form factor. Among these, the axial form factor $F_A(q^2)$ will be the main focus of our study. A graphical representation of the axial-vector current is provided in Fig. 1. $F_A(q^2)$ is represented as a gray blob, and we can see it encodes information on the hadronic structure of the nucleon. This process is known to involve the exchange of the $a_1(1260)$ axial resonance ($J^{PC} = 1^{++}$) [5], which implies the existence of a single pole in the $F_A(q^2)$ modelling. However, the most frequently used parametrization for the axial form factor is the dipole ansatz introduced by Lewellyn-Smith [6] to explain the quasielastic neutrino-nucleon $\nu_\mu n \to \mu p$ scattering data

$$F_A(Q^2) = \frac{g_A}{\left(1 + Q^2/m_A^2\right)^2}, \quad Q^2 \equiv -q^2 \geq 0, \quad (3)$$

where $g_A = F_A(0)$ is a normalization constant that represents the strength of the interaction of the axial current with the nucleon at zero momentum transfer (experimentally well-known from from neutron β decays, $g_A = 1.2732$ [5]) and $m_A = 1230$ MeV is the mass of the $a_1(1260)$ meson. Although this approach respects the expected $1/Q^4$ fall-off at high-energies that perturbative QCD dictates [7, 8], it also introduces an unnatural artificial bias connecting high-and-low regions of Q^2.

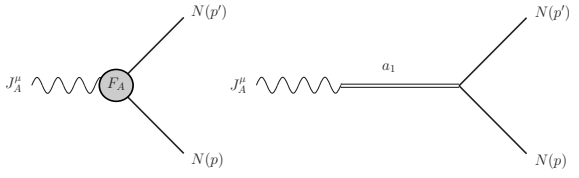

FIG. 1: Feynman diagrams representing the axial current coupling to nucleons. The left diagram encodes the interaction in terms of the axial form factor F_A, while the diagram on the right illustrates the a_1 resonance contribution to the axial-vector current matrix element between nucleon states.

The expansion of the axial form factor around $Q^2 = 0$ is written as

$$F_A(Q^2) = g_A - \frac{1}{6}g_A\langle r_A^2\rangle Q^2 + \mathcal{O}(Q^4), \quad (4)$$

where $\langle r_A^2\rangle$ is the mean square axial radius. In our analysis, this magnitude will be the key quantity extracted from the experimental data. Since the definition of the slope in Eq. 4 is model-independent, $\langle r_A^2\rangle$ will allow us to compare our results with those obtained in other approaches.

In Table I we provide a summary of state-of-the-art extractions of the axial mass and radius. As shown, there are some discrepancies among the results reported by different collaborations. In this work, we employ Padé approximants to investigate and clarify these tensions.

TABLE I: Axial masses and mean squared radius reported by recent quasielastic neutrino-nucleon scattering experiments, $\nu_\mu n \to \mu p$.

Reference	m_A[GeV]	$\langle r_A^2\rangle$ [fm^2]
K2K [9]	1.20 ± 0.12	0.32 ± 0.06
NOMAD [10]	1.05 ± 0.06	0.42 ± 0.05
MiniBooNE [11]	1.35 ± 0.17	0.26 ± 0.06
MINERvA [12]	0.99	0.48
MINOS [13]	$1.23^{+0.13}_{-0.09}$	$0.31^{+0.07}_{-0.05}$

III. PADÉ APPROXIMANTS

When working with perturbative QCD, solutions often emerge as a power series that either converges very slowly or diverges altogether. In such cases, Taylor expansions present two main setbacks: first, computing the coefficients is not a trivial task; second, its range of applicability is often unknown and difficult to assess. Moreover, the divergence of a series typically signals the presence of singularities (i.e. poles, cuts, etc.) in the underlying function, and polynomials are unable to reproduce them in the whole convergence range.

With these limitations in mind, we turn to a considerably more effective method of approximation that will allow us to accelerate the convergence of our function and hopefully reproduce its poles: *Padé Approximants* (PAs) [4].

Given a complex-valued function $f(z)$ with a well defined power series around the origin and a radius of convergence $|z| = R$,

$$f(z) = \sum_{n=0}^{\infty} c_n z^n, \quad (5)$$

its PA of order $N + M$ is a rational function defined as

$$P_M^N(z) = \frac{\sum_{n=0}^{N} r_n z^n}{\sum_{m=0}^{M} q_m z^m}, \quad (6)$$

where coefficients r_n and q_m are are uniquely determined by requiring that $P_M^N(z)$ matches the power series expansion of $f(z)$ up to the z^{N+M} term :

$$|f(z) - P_M^N(z)| = \mathcal{O}(z^{N+M+1})\,. \tag{7}$$

For convergent series, PAs typically exhibit a slightly faster rate of convergence than the corresponding Taylor series, although the improvement is often negligible. Their true power, however, lies in handling divergent series, where they can provide meaningful approximations even when the Taylor expansion fails.

Take, for example, the function

$$f(z) = \frac{1}{z}\log(z+1). \tag{8}$$

As shown in Fig. 2, while its Taylor series diverges for $|z| \geq 1$, PAs are capable of accurately reproducing the function throughout its entire domain. Furthermore, if we compare the relative error at a given order of approximation, we can clearly see that the values obtained with PAs fall much quicker than the ones corresponding to the Taylor series (Fig. 3).

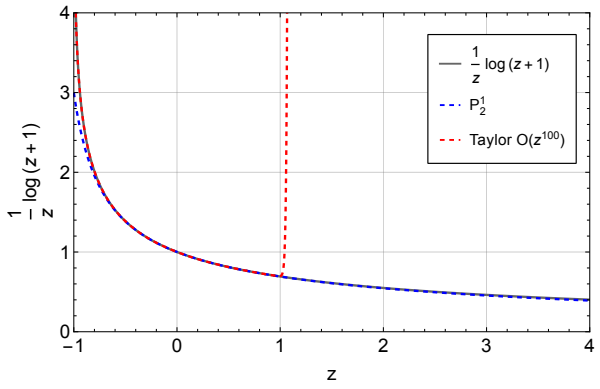

FIG. 2: Convergence behaviour of the $P_2^1(z)$ PA (dashed blue line) as opposed to the Taylor series of order $\mathcal{O}(z^{100})$ (dashed red line).

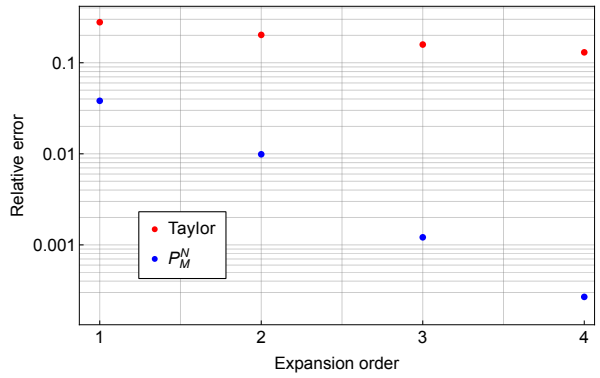

FIG. 3: Relative error obtained from the approximation of the function in Eq. 8 with a Taylor expansion of order n (red) and a PA of total order $N+M$ (blue). Note that Eq. 7 allows us to directly compare these approximation orders.

IV. DETERMINATION OF THE AXIAL RADIUS $\langle r_A^2 \rangle$

As mentioned in Sec. II, we know that, at the very least, $F_A(Q)$ presents one pole associated with the $a_1(1260)$ axial ressonance. To incorporate this information, we express the denominators of the PAs in terms of their roots — that is,

$$P_M^N(Q^2) = \frac{1 + r_1 Q^2 + \cdots + r_N (Q^2)^N}{(1 + Q^2/m_A^2)(1 + q_1 Q^2)\cdots(1 + q_{M-1} Q^2)}\,. \tag{9}$$

This allows us to fix one of the poles to match the resonance mass of the a_1 meson ($m_A = 1,230\,\text{GeV}$). Note that we can normalize our PA by fixing $r_0 = 1$ without loss of generality.

To perform the fit, we use the NonlinearModelFit function provided by Mathematica, which enables us to determine both the central value and the uncertainty of each parameter r_n, q_m, along with the covariance matrix. We start by performing fittings to three datasets from Lattice QCD predictions [2, 3], and subsequently include data from pion electroproduction experiments [1] to carry out a joint fit for a more complete analysis. In Fig. 4 we present the resulting parametrization of the PA $P_2^2(Q^2)$ to all the data (other examples of fits obtained with different PAs and datasets are shown in Appendix A).

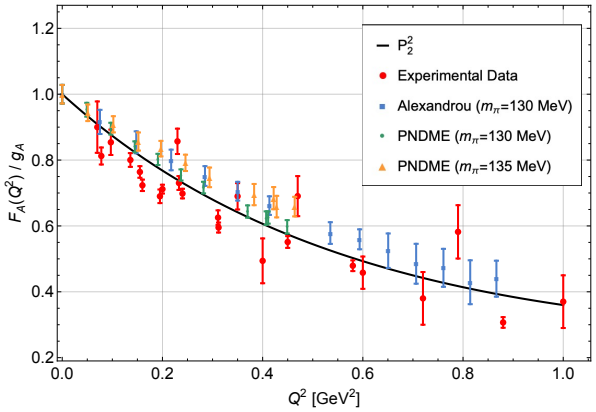

FIG. 4: Normalized $F_A(Q^2)$ Lattice QCD and pion electroproduction data fitted using the $P_2^2(Q^2)$ PA. The former are represented by the blue square, green point and orange triangle markers, and are labeled with the names of the collaborations they correspond to. The latter are represented as red points and have been labeled as *experimental data*.

It is important to note that, given the finite amount of data available, the precision of the approximation is inherently limited. Beyond a certain order, the uncertainties in the fitted parameters grow significantly, reducing the ability of the PA to reflect meaningful physical quantities. Taking this factor into account, we only compute PAs up to total order 5 (i.e. $N + M \leq 5$).

As established in Eq. 7, the power series of the PAs and the function they approximate ($F_A(Q^2)$ in our case)

agree up to order $N + M + 1$. This property, together with the Taylor expansion of the axial form factor given in Eq. 4, allows us to compute the axial radius from the fitted PA via

$$\langle r_A^2 \rangle = -6 \, \frac{d}{dQ^2} P_M^N(Q^2) \Big|_{Q^2=0} , \tag{10}$$

where we have taken into account that the dataset is already normalized, hence why g_A does not appear explicitly. Moreover, to express the axial radius in femtometers squared, we apply the unit conversion $1\,\text{GeV}^{-2} = (197,326)^2 \times 10^{-6}\,\text{fm}^2$, with $197,326\,\text{MeV}\cdot\text{fm}$ being the value of $\hbar c$.

A. Lattice QCD

For the Lattice QCD predictions, we perform a total of eleven fittings with Padé sequences of the type $P_1^N(Q^2), P_2^N(Q^2), P_3^N(Q^2)$ and $P_4^N(Q^2)$ and we reach $N = 3$, $N = 2$, $N = 2$ and $N = 0$ respectively. We cannot use higher order PAs for the reasons aforementioned.

The results of computing the mean squared axial radius are shown in Fig. 5 ($P_1^N(Q^2)$ series) and Fig. 6 (all sequences). Note that, since r_0 and the first pole in the denominator are fixed, the $P_1^0(Q^2)$ PA does not present any parameters to adjust, and therefore its corresponding $\langle r_A^2 \rangle$ does not have any uncertainty. Furthermore, the $P_3^1(Q^2)$ and $P_4^0(Q^2)$ parametrizations exhibit degenerated roots in the denominator, leading to a highly correlated set of parameters. This is reflected in the covariance matrix, which displays large off-diagonal elements and consequently increases the propagated errors. Since this is not a natural source of error, we proceed with the axial radius calculation but assign its uncertainty manually, guided by the spread of values obtained from PAs with the same order in the denominator.

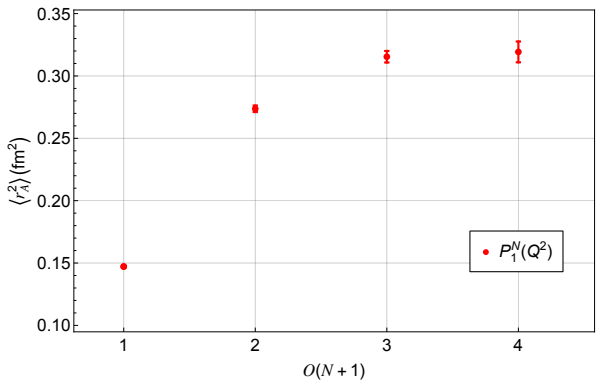

FIG. 5: Mean squared axial radius convergence pattern obtained with the $P_1^N(Q^2)$ sequence fitted to the Lattice QCD predictions.

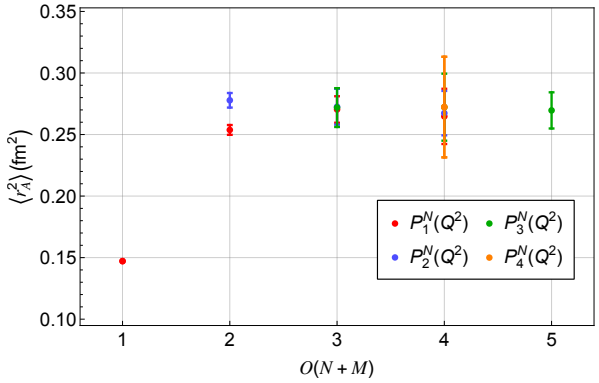

FIG. 6: Convergence pattern of the mean squared axial radius for the PA series $P_1^N(Q^2)$ (red), $P_2^N(Q^2)$ (blue), $P_3^N(Q^2)$ (green) and P_4^N (orange) fitted to the Lattice QCD dataset.

B. Lattice QCD + pion electroproduction

The fitting procedure applied to the combined Lattice QCD and pion elecroproduction datasets is the same as that used for the Lattice QCD predictions alone. The pion electroproduction data presents a large dispersion of its values, so before performing the fit we compute the weighted average of any points that share the same Q^2. Despite this, we are only able to reach an order of approximation up to four. The resulting $\langle r_A^2 \rangle$ values are shown in Fig. 7.

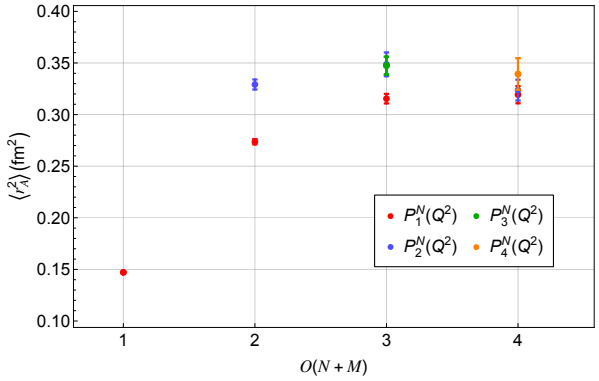

FIG. 7: Convergence pattern of the mean squared axial radius for the PA series $P_1^N(Q^2)$ (red), $P_2^N(Q^2)$ (blue), $P_3^N(Q^2)$ (green) and P_4^N (orange) fitted to the Lattice QCD and pion electroproduction datasets.

We have also performed an additional fit to the pion electroproduction data; however, due to the large dispersion of the dataset, the resulting output is also highly dispersed. The mean squared axial radius values obtained can be found in Appendix B.

In Table II we collect the weighted mean values of the $\langle r_A^2 \rangle$ obtained with the higher order PA of each sequence for each case. We can compare our results to the ones summarized in Table I. For the Lattice QCD dataset, it

appears our predictions best align with the MiniBoonNE values, while the combined data seems to agree with the K2K collaboration. The pion electroproduction results seem to lean toward the NOMAD predictions, although the two values show substantial differences.

TABLE II: Weighted average of the $\langle r_A^2 \rangle$ values obtained with the Lattice QCD and pion electroproduction datasets and a combination of the two.

Dataset	$\langle r_A^2 \rangle$ [fm^2]
Lattice QCD	0.268 ± 0.010
Pion electroproduction	0.405 ± 0.009
Lattice QCD +pion electroproduction	0.324 ± 0.006

V. CONCLUSIONS

In this work, we have studied the axial-vector form factor of the nucleon, an object of high fundamental interest in nuclear and particle physics. We have used Padé approximants as a novel approach its parametrization. PAs are a systematic, model-independent method that allows for the precision of the fit to increase as more data becomes available, reducing the outcome parameters' uncertainties. This flexibility represents a great advantage over the most standarized parametrization — the dipole ansatz.

Using data from Lattice QCD predictions and pion electroproduction experiments, we have been able to compute the mean squared axial radius up to various orders of approximation. We have obtained $\langle r_A^2 \rangle = (0.268 \pm 0.010)\,\text{fm}^2$ from the Lattice QCD predictions, $\langle r_A^2 \rangle = (0.405 \pm 0.009)\,\text{fm}^2$ from the pion electroproduction data and $\langle r_A^2 \rangle = (0.324 \pm 0.006)\,\text{fm}^2$ from the combined datasets. Our results seem to present a strong alignment with the MiniBoonNE and K2K collaborations for the Lattice QCD and combined datasets respectively.

The field this work has touched on is an open one, and we believe the adaptability to the experimental data PAs provide represents a promising direction for future research.

Acknowledgments

I would like to thank my advisor, Sergi Gonzàlez-Solís for his guidance and encouragement throughout this project. I have learned a lot from him during this journey. I am also grateful to my parents, my brother and my friends for brightening my days the way they do.

[1] V. Bernard, L. Elouadrhiri, and U.-G. Meissner, "Axial structure of the nucleon: Topical Review," J. Phys. G, vol. 28, pp. R1–R35, 2002.
[2] C. Alexandrou, M. Constantinou, K. Hadjiyiannakou, K. Jansen, C. Kallidonis, G. Koutsou, and A. Vaquero Aviles-Casco, "Nucleon axial form factors using $N_f = 2$ twisted mass fermions with a physical value of the pion mass," Phys. Rev. D, vol. 96, no. 5, p. 054507, 2017.
[3] R. Gupta, Y.-C. Jang, H.-W. Lin, B. Yoon, and T. Bhattacharya, "Axial Vector Form Factors of the Nucleon from Lattice QCD," Phys. Rev. D, vol. 96, no. 11, p. 114503, 2017.
[4] G. A. Baker and P. Graves-Morris, Padé Approximants. Cambridge Univ. Press, 1996.
[5] S. Navas et al., "Review of particle physics," Phys. Rev. D, vol. 110, no. 3, p. 030001, 2024.
[6] C. H. Llewellyn Smith, "Neutrino Reactions at Accelerator Energies," Phys. Rept., vol. 3, pp. 261–379, 1972.
[7] S. J. Brodsky and G. R. Farrar, "Scaling Laws for Large Momentum Transfer Processes," Phys. Rev. D, vol. 11, p. 1309, 1975.
[8] C. E. Carlson and J. L. Poor, "The Nucleon Axial Vector Form-factor in Perturbative QCD," Phys. Rev. D, vol. 34, p. 1478, 1986.
[9] R. Gran et al., "Measurement of the quasi-elastic axial vector mass in neutrino-oxygen interactions," Phys. Rev. D, vol. 74, p. 052002, 2006.
[10] V. Lyubushkin et al., "A Study of quasi-elastic muon neutrino and antineutrino scattering in the NOMAD experiment," Eur. Phys. J. C, vol. 63, pp. 355–381, 2009.
[11] A. A. Aguilar-Arevalo et al., "First Measurement of the Muon Neutrino Charged Current Quasielastic Double Differential Cross Section," Phys. Rev. D, vol. 81, p. 092005, 2010.
[12] L. Fields et al., "Measurement of Muon Antineutrino Quasielastic Scattering on a Hydrocarbon Target at E$\nu\sim$3.5 GeV," Phys. Rev. Lett., vol. 111, no. 2, p. 022501, 2013.
[13] P. Adamson, I. Anghel, A. Aurisano, G. Barr, M. Bishai, A. Blake, G. Bock, D. Bogert, S. Cao, C. Castromonte, et al., "Study of quasielastic scattering using charged-current ν μ-iron interactions in the minos near detector," Physical Review D, vol. 91, no. 1, p. 012005, 2015.

El factor de forma axial del nucleó amb aproximants de Padé

Author: Laia Asiain Peracaula, lasiaipe7@alumnes.ub.edu
Facultat de Física, Universitat de Barcelona, Diagonal 645, 08028 Barcelona, Spain.

Advisor: Sergi Gonzàlez-Solís de la Fuente, sergig@fqa.ub.edu

Resum: Aquest treball estudia el factor de forma axial del nucleó, $F_A(Q^2)$, utilitzant aproximants de Padé com una alternativa a la parametrització dipolar tradicional. Aquesta metodologia permet tenir en compte l'estructura de la ressonància $a_1(1260)$ a l'hora de fer l'ajust de les dades experimentals. Per altra banda, en ser un model sistemàtic, els aproximants de padé ens permeten obtenir resultats més precisos i amb errors més petits a mesura que incorporem més dades experimentals a l'ajust. Hem ajustat dades extretes de prediccions de Lattice QCD i experiments d'electroproducció de pions per calcular el radi quadràtic mig axial, $\langle r_A^2 \rangle$. Els resultats obtinguts són $\langle r_A^2 \rangle = (0.268 \pm 0.010)\,\mathrm{fm}^2$ per les dades de Lattice QCD, $\langle r_A^2 \rangle = (0.405 \pm 0.009)\,\mathrm{fm}^2$ per les dades d'electroproducció de pions, i $\langle r_A^2 \rangle = (0.324 \pm 0.006)\,\mathrm{fm}^2$ pels dos conjunts de dades combinats. Finalment, comparem aquests valors amb els obtinguts en altres estudis, com els de les col·laboracions K2K o MiniBoonNE.
Paraules clau: Factor de forma axial, Aproximants de Padé, Lattice QCD, Electroproducció de pions, Estructura del nucleó
ODSs: Educació de qualitat

Objectius de Desenvolupament Sostenible (ODSs o SDGs)

El contingut d'aquest TFG, elaborat en el marc del grau universitari de Física, es vincula amb l'ODS 4, i en particular amb la fita 4.4, ja que contribueix a la formació acadèmica superior i al desenvolupament de competències tècniques en l'àmbit científic.

Appendix A: Additional fitting examples

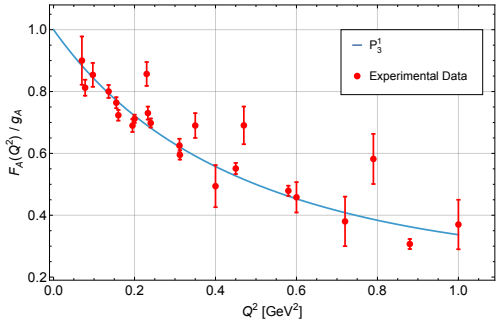

FIG. 8: Normalized $F_A(Q^2)$ pion electroproduction data fitted using the $P_3^1(Q^2)$ PA.

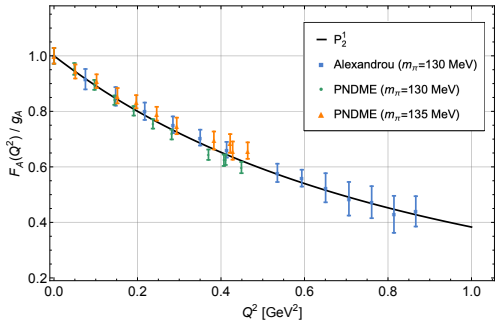

FIG. 9: Normalized $F_A(Q^2)$ Lattice QCD data fitted using the $P_2^1(Q^2)$ PA. Each marker corresponds to one of the collaborations from which the data has been obtained.

Figs. 8, 9 show the parametrization of pion electroproduction and Lattice QCD data with two different PAs ($P_3^1(Q^2)$ and $P_2^1(Q^2)$).

Appendix B: Pion electroproduction $\langle r_A^2 \rangle$ convergence

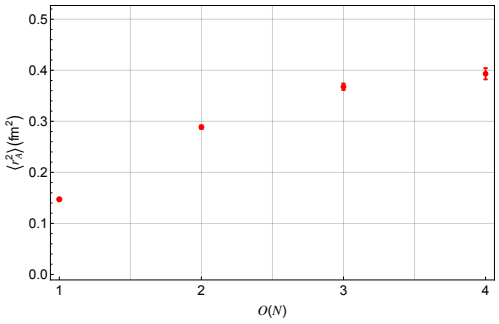

FIG. 10: Mean squared axial radius convergence pattern obtained with the $P_1^N(Q^2)$ sequence fitted to the pion electroproduction data.

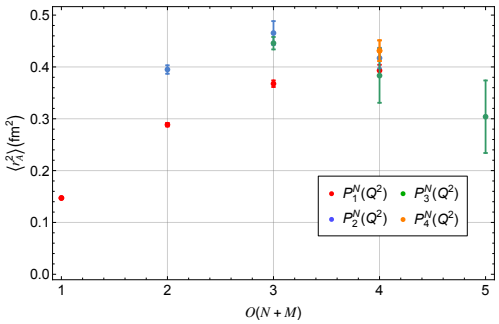

FIG. 11: Convergence pattern of the mean squared axial radius for the PA series $P_1^N(Q^2)$ (red), $P_2^N(Q^2)$ (blue), $P_3^N(Q^2)$ (green) and P_4^N (orange) fitted to the pion electroproduction data.

Figs. 10, 11 show the results of computing the mean squared axial radius with the pion electroproduction data. Although it appears the $P_N^1(Q^2)$ sequence shows a stable convergence pattern, if we analize the results obtained from the rest of the series we can see they present significant dispersion.